Performance capabilities of middle-atmosphere temperature lidars: comparison of Na, Fe, K, Ca, Ca^+, and Rayleigh systems

Chester S. Gardner

The measurement accuracies of modern resonance fluorescence and Rayleigh temperature lidars are limited primarily by photon noise. The narrowband three-frequency fluorescence technique is shown to perform within a few decibels of the theoretical optimum at night for both temperature and wind observations. These systems also exhibit good performance during the day because the fluorescence wavelengths of Na, Fe, K, Ca, and Ca^+ all correspond to strong solar Fraunhofer lines, where sky brightness is attenuated by a factor of 5 or more. Whereas Na systems achieve the highest signal-to-noise ratios for mesopause region observations (80–105 km), the three-frequency Fe system is attractive because it performs well as both a fluorescence and a Rayleigh lidar throughout the middle atmosphere at approximately 25–110 km.

OCIS codes: 010.3640, 280.1310, 280.3640, 290.5870, 120.0280, 120.6780.

1. Introduction

Since the invention of the ruby laser in 1960, numerous lidar systems have been developed to study the structure of the middle atmosphere (30–110 km). The Rayleigh technique has evolved from the searchlight-based systems deployed in the early 1950s to measure stratospheric temperatures and aerosols[1–3] into powerful UV-laser-based systems that can now measure winds in the stratosphere[4] and temperatures to altitudes in excess of 85 km.[5] Resonance fluorescence techniques have also evolved from the broadband dye laser systems designed to measure Na densities[6] into sophisticated narrowband systems that are now capable of measuring atmospheric temperatures and winds throughout the mesopause region[7] (80–105 km). These instruments rely on the temperature (thermal broadening) and frequency dependence (Doppler shift) of the fluorescence cross sections of mesospheric metals such as Na,[8] Fe,[9] and K.[10] By accurately tuning a narrowband pulsed laser to three or more frequencies within the thermally broadened fluorescence line, one can infer species density, atmospheric temperature, and radial winds along the beam path. When these lasers are coupled to large steerable telescopes, accuracies approaching ± 1 K and ± 1 m/s with resolutions of a few hundred meters and a few minutes are now achieved routinely with the largest, most powerful systems.

Rayleigh and resonance fluorescence techniques have matured until the fundamental uncertainties in the temperature and wind measurements are due to photon noise, which is related to the statistical fluctuations of the received signal and background noise. The molecular or Rayleigh backscatter signal level is proportional to atmospheric density and inversely proportional to the fourth power of the wavelength. Assuming that other factors are equal, the strongest signals and hence the best accuracies and the greatest altitude coverage are achieved with systems that utilize the shortest wavelengths in the near UV. The fluorescence backscatter signal is proportional to the species density and cross section. Because of its relatively large natural abundance and large cross section, Na has the clear advantage, which is why so much effort has been focused on developing suitable laser technologies for Na lidar systems.

Background noise is a significant issue for daytime observations, for which recent research efforts have concentrated on characterizing thermal tides[11,12] and the summer middle atmosphere at high latitudes.[13]

C. S. Gardner (cgardner@uillinois.edu) is with the Department of Electrical and Computer Engineering, University of Illinois at Urbana—Champaign, Urbana, Illinois 61801-2307.

Received 12 February 2004; revised manuscript received 4 May 2004; accepted 21 May 2004.

0003-6935/04/254941-16$15.00/0

Table 1. Atomic Parameters of Mesospheric Metals at $T = 200$ K and $V = 0$ m/s

Species	Central Wavelength λ_S (nm)	Atomic Mass ($\times 10^{-23}$ g)	A_{21} (MHz)	Doppler Width, σ_D (MHz)	$\lambda_S \sigma_D$ (m/s)	Peak Cross Section, σ_S ($\times 10^{-12}$ cm^2)
Na (D_2)	588.995	3.8177	61.6	456.54	268.97	14.87
Fe	371.994	9.2738	16.3	463.79	172.58	0.944
K (D_1)	769.896	6.4923	38.2	267.90	206.26	13.42
Ca	422.673	6.6556	218	481.96	203.71	38.48
Ca^+	393.366	6.6556	147	517.87	203.71	13.94

Resonance fluorescence lidars have a distinct advantage during daytime because the resonance lines of Na, Fe, K, Ca, and Ca^+ all correspond to strong solar Fraunhofer lines in which the sky brightness is attenuated by a factor of ~5 or more.

Signal levels are also proportional to the laser power and the aperture area of the receiving telescope. Laser technology has improved considerably during the past 15 years such that tunable, frequency-stable narrowband systems that are capable of producing several watts of average power are now available for probing each of the mesospheric metal species. The frequency-stabilized Nd:YAG lasers commonly used for Rayleigh lidars can be obtained commercially with average power levels of several tens of watts. Whereas the complexity of these systems varies, the relative performance of resonance fluorescence and Rayleigh lidars now appears to be dictated more by natural factors than by technology limitations.

In this paper we analyze and compare the performance of modern middle-atmosphere temperature lidars. The goal is to quantify the strengths and weaknesses of each technique to guide the development of future systems that are optimized for specific scientific applications. Whereas current systems have demonstrated impressive measurement capabilities, most require a laboratory environment for their operation, a restriction that has limited wide-scale deployment. Furthermore, there is still a notable lack of daytime observations, which are crucial for fully characterizing the thermal structure and dynamics of the middle atmosphere.

2. Principle of Operation

Atomic fluorescence spectra have been studied in considerable detail both theoretically and experimentally. The spectra of isolated lines can be modeled as the convolution of the Lorentzian line shape associated with lifetime broadening and the Gaussian line shape associated with thermal broadening.[14] Because thermal broadening (~300–~500 MHz rms) is considerably larger than lifetime broadening (~10 MHz FWHM) for mesospheric Na, Fe, K, Ca, and Ca^+, their spectra can be approximated as Gaussian line shapes centered at each resonance line.[15,16]

The atomic parameters for mesospheric Na, Fe, K, Ca, and Ca^+ are summarized in Table 1. Fe, Ca, and Ca^+ have no hyperfine structure, so a single thermally broadened Gaussian line is an excellent model for their spectra. The Na D_2 line and the K D_1 line have complex hyperfine structures. More than 1.7 GHz separates the Na D_{2a} and D_{2b} peaks, and the rms thermal broadening is approximately 460 MHz at 200 K. A Gaussian line shape can be used to approximate each peak. For the purposes of modeling the error performance of the narrowband Na temperature lidar, the small contribution from the D_{2b} line can be neglected.

Only ~460 MHz separates the K D_{1a} and D_{1b} lines, and the rms thermal broadening is approximately 270 MHz. Whereas each line is well modeled by a Gaussian line, the composite spectrum is only approximately Gaussian. Papen *et al.*[16] showed how a modified Gaussian line profile can be used to approximate the K spectrum. For simplicity, we use the simpler thermally broadened Gaussian line shape in our analysis. This approach results in slightly more optimistic estimates of the temperature and wind performance for the K lidar. This is adequate for comparing the performances among lidar types. However, in practice, detailed quantum-mechanical models of the spectra are used to process the lidar temperature and wind data for each species and to determine the accuracy of the measurements.[10,15]

The analysis of K,[10,17] Ca, and Fe (Ref. 18) lidar data is further complicated by the presence of several natural isotopes whose relative concentrations are listed in Table 2. Although the atmospheric concentrations of the minor isotopes are small, they do affect

Table 2. Naturally Occurring Isotopes of Na, K, Fe, and Ca[a]

Isotope	Natura Abundance (Atomic %)	Nuclear Spin (I)	Magnetic Moment (m/m_N)
^{23}Na	100	3/2	2.217520
^{54}Fe	5.85	0	0
^{56}Fe	91.75	0	0
^{57}Fe	2.12	1/2	0.09062294
^{58}Fe	0.28	0	0
^{39}K	93.26	3/2	0.3914658
^{40}K	0.012	4	−1.298099
^{41}K	6.73	3/2	0.2148699
^{40}Ca	96.94	0	0
^{42}Ca	0.65	0	0
^{43}Ca	0.14	7/2	−1.31727
^{44}Ca	2.09	0	0
^{46}Ca	0.004	0	0
^{48}Ca	0.19	0	0

[a]For further information see http://www.webelements.com/webelements/.

the temperatures and velocities derived from narrowband lidar data because their fluorescence lines can be shifted by as much as several hundred megahertz relative to the dominant isotope. The natural isotopes must be included in the modeled fluorescence spectra that are used to process the lidar temperature and wind data.[10,17,18] However, they have a negligible effect on the modeling of system error performance associated with photon noise, so we ignore isotope effects in the following analyses.

For an isolated line excited by a broadband light source, the fluorescence spectrum, in photon counts per hertz, is given by

$$S(f) = \frac{N_S}{\sqrt{2\pi}\sigma_D} \exp[-(f - f_S + V_R/\lambda_S)^2/2\sigma_D{}^2], \quad (1)$$

where

$$\sigma_D{}^2 = \frac{k_B T}{\lambda_S{}^2 m_S} = \gamma T,$$

$$\gamma = \frac{k_B}{\lambda_S{}^2 m_S}, \quad (2)$$

N_S is the total photon count, f_S is the center frequency of the species resonance line [Hz], λ_S is the wavelength of the species resonance line [m], V_R is the radial velocity relative to the observer [m/s], k_B is Boltzmann's constant (1.38×10^{-23} J/K), T is the temperature [K], and m_S is the atomic mass of species [g].

V_R is assumed to be positive whenever the species is moving away from the observer. One determines temperature and velocity by measuring the width and the Doppler shift of the spectrum. For purely Gaussian spectra observed in the absence of background noise by an ideal receiver that measures precisely the frequency of each detected photon, the maximum-likelihood estimators for temperature and radial velocity are proportional to the mean photon frequency minus f_S and the mean-square frequency deviation, respectively (Appendix A). Both are identical to the minimum mean-square-error estimators, so they represent the theoretically optimum measurement of these parameters for nighttime observations. For the ideal receiver that employs maximum-likelihood processing, the temperature and velocity errors are given by

$$\Delta T_{\mathrm{rms}} \approx \frac{\sqrt{2}T}{\sqrt{N_S}} = \frac{\sqrt{2}T}{\sqrt{\mathrm{SNR}_S}}$$

$$\Delta V_{\mathrm{rms}} \approx \frac{\lambda_S \sigma_D}{\sqrt{N_S}} = \frac{\lambda_S \sigma_D}{\sqrt{\mathrm{SNR}_S}},$$

theoretical minima at night. (3)

Of course, it is not technically feasible to build such a receiver, so the error performance of practical lidars will not be so good as the theoretical minima given by relations (3). However, these error limits provide an important standard of comparison for assessing the performances of the suboptimum systems that are in use today.

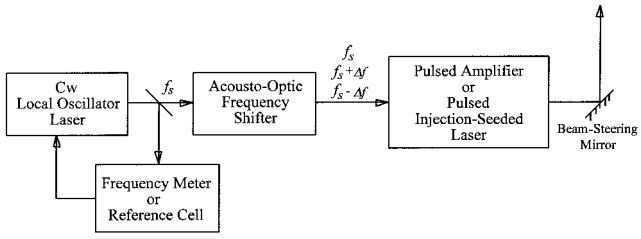

Fig. 1. Basic laser configuration for a modern resonance fluorescence wind–temperature lidar.

Gibson *et al.*[19] used a narrowband dye laser to scan through the Na D_2 fluorescence spectrum to deduce the temperature near the peak of the mesospheric Na layer (~90 km). Six years later, Fricke and von Zahn[20] employed improved laser technology to routinely measure temperature profiles throughout the Na layer. An important technical advance occurred in 1990 when She *et al.*[21] used a system that comprised a cw ring laser and a pulsed amplifier to tune accurately between two Doppler-free features in the Na D_2 line. This approach ensured accurate tuning of the laser, which eliminated a major source of error in the temperature measurements. Shortly thereafter, Bills *et al.*[22] employed a similar laser system and three- and four-frequency techniques to measure both radial wind and temperature profiles throughout the mesopause region, using Na as the tracer.

Another important technical advance occurred in 1994 when She and Yu[23] developed an acousto-optic (AO) modulator to upshift and downshift the output frequency of a cw ring laser by several hundred megahertz. The ring laser was permanently locked to a Doppler-free hyperfine feature near the Na D_{2a} peak. The AO modulator, in combination with a frequency-locked ring laser and a pulsed dye amplifier, generated laser pulses with three precisely controlled frequencies within the Na resonance line such that both temperature and winds could be measured. Although it has not yet been demonstrated experimentally, the same three-frequency approach could be used for wind and temperature measurements with Ca and Ca^+ used as tracers because the laser and the amplifier can operate at those resonance lines if a different laser dye is used with each. Recently Friedman *et al.*[17] adopted a similar approach for mesospheric K. They used an AO modulator to upshift and downshift the output of a diode laser that was locked to a Doppler-free feature of the K D_1 line. These signals were then used to injection seed a pulsed alexandrite ring laser. One could also use a similar approach for Fe and Ca^+ by frequency doubling the output of the IR alexandrite laser to probe the 372-nm (or 386-nm) Fe line or the 393-nm Ca^+ line.

The basic laser configuration for three-frequency resonance fluorescence wind–temperature lidars is illustrated in Fig. 1. The cw local oscillator (ring dye

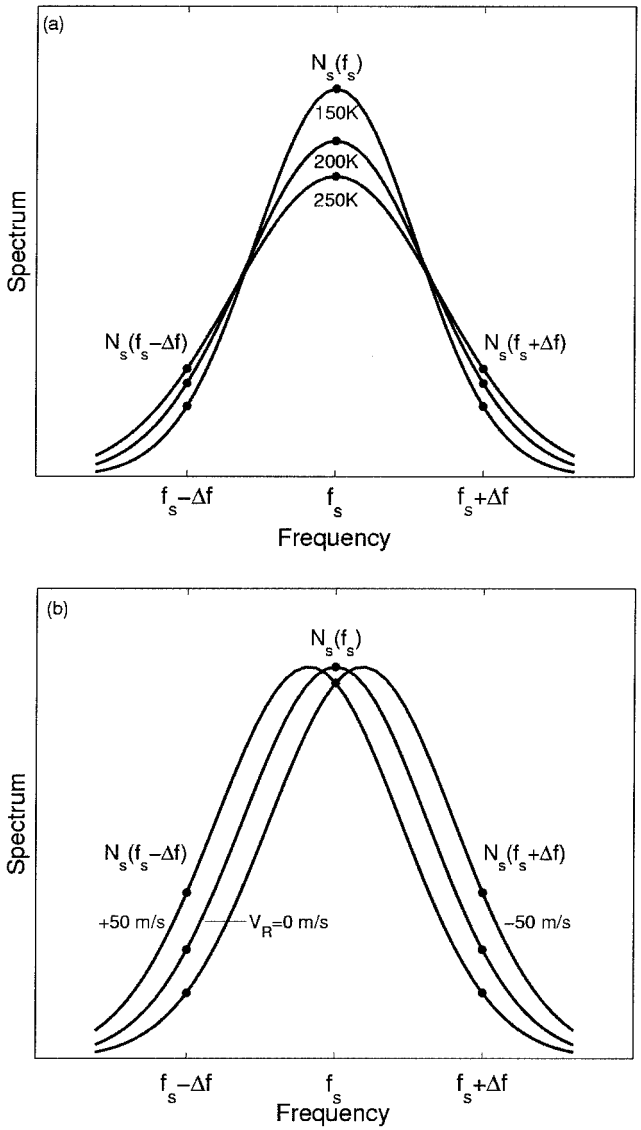

Fig. 2. Spectrum of an isolated fluorescence line plotted for several values of (a) temperature and (b) radial velocity. Measurements of the backscattered signal are made by tuning the laser to line center frequency f_S and to the wings of the spectrum at $f_S \pm \Delta f$, as indicated. The temperature and radial velocity are calculated by combining the measured signals according to Eqs. (6), (7), (24), and (25).

laser for Na, Ca, and Ca^+; diode laser for K and Fe) is locked to the peak of the species resonance line (f_S). The output is then shifted by an AO modulator to generate the remaining two frequencies ($f_S \pm \Delta f$), which are used to probe the wings of the line. These signals are either pulse amplified or used to injection seed a pulsed laser. The measurement principle is illustrated in Fig. 2. The backscattered signal is measured sequentially at each of the three frequencies. The ratio of the sum of the wing measurements at $f_S \pm \Delta f$ to the peak measurement at f_S is a sensitive function of temperature. The ratio of the wing measurements is a sensitive function of radial velocity. The actual temperature and wind metrics are a bit more complicated than these simple ratios (see Section 3 below), but the measurement principle is the same.

The wing frequencies and the dwell times at each frequency can be chosen to minimize the error. The optimum parameters are different for temperature and wind observations, and they are different for day and night observations, as is illustrated in Section 3, in which we analyze the system's performance in detail. We then use the key results to compare the performances of Na, Fe, K, Ca, and Ca^+ lidars.

The Fe Boltzmann technique was proposed as an alternative for measuring mesopause region temperatures that has the advantage of employing simpler broadband laser technology.[24] One infers temperature by measuring the ratio of the populations in the $J = 3$ and $J = 4$ sublevels in the ground-state manifold of atomic Fe; this involves measuring the Fe densities at the 372- and 374-nm resonance lines. Because it operates in the near UV, the Fe lidar also performs well as a Rayleigh lidar and can provide temperature profiles throughout the stratosphere, the mesosphere, and the lower thermosphere. The technique has been used to make temperature observations from research aircraft and at remotes sites such as the South Pole.[13,25] In Section 3 the performance of the Fe Boltzmann lidar is compared with that of conventional Rayleigh lidars and with the three-frequency narrowband fluorescence technique.

3. Error Analysis for Temperature Measurements

The backscattered signal level for a narrowband lidar tuned to an isolated resonance line such as Fe (we ignore isotope shifts) is given by

$$N_S(f) = N_S \exp[-(f - f_S + V_R/\lambda_S)^2/2\sigma_\lambda^2], \quad (4)$$

where

$$\sigma_\lambda^2 = \sigma_L^2 + \frac{k_B T}{\lambda_S^2 m_S} = \sigma_L^2 + \gamma T, \quad (5)$$

σ_L [Hz] is the rms laser line width, f [Hz] is the laser frequency, and the remaining parameters are defined immediately following Eqs. (2). For simplicity we assume that the laser linewidth is negligible compared with thermal broadening (i.e., that $\sigma_L \ll \sigma_D$), although this is not essential for measuring temperature and winds.

One determines temperature by measuring the backscattered signal at three frequencies within the resonance line, preferably centered about the line peak. Let f_S denote the line center frequency and Δf denote the offset frequency. Measurements of the species backscatter are made at f_S and at $f_S \pm \Delta f$. These measurements are normalized by the Rayleigh counts at ~40-km altitude and combined as follows to form the temperature metric:

$$R_T = \frac{N_S^2(f_S)}{N_S(f_S + \Delta f) N_S(f_S - \Delta f)} = \exp(\Delta f^2/\sigma_\lambda^2). \quad (6)$$

Because the mean Rayleigh signals are nominally identical at all three frequencies, they do not appear in Eq. (6). Notice that this metric is independent of the Doppler shift caused by the radial winds. It is also insensitive to laser tuning errors.

The temperature is derived from Eq. (6) as follows:

$$T = \frac{\Delta f^2}{\gamma \ln R_T} - \sigma_L{}^2/\gamma. \tag{7}$$

The rms temperature error is given by

$$\begin{aligned}\Delta T_{\mathrm{rms}}|_{3-\mathrm{freq}} &= T\left(\frac{\sigma_\lambda}{\Delta f}\right)^2 \frac{\Delta R_T}{R_T} \\ &= T\left(\frac{\sigma_\lambda}{\Delta f}\right)^2 [1/\varepsilon \mathrm{SNR}_+ + 1/\varepsilon \mathrm{SNR}_- \\ &\quad + 4/(1-2\varepsilon)\mathrm{SNR}_S]^{1/2} \\ &= T\left(\frac{\sigma_\lambda}{\Delta f}\right)^2 \left[\frac{2}{\varepsilon \mathrm{SNR}_\pm} + \frac{4}{(1-2\varepsilon)\mathrm{SNR}_S}\right]^{1/2} \\ &= \frac{T}{\sqrt{\mathrm{SNR}_S}} 2\left(\frac{\sigma_\lambda}{\Delta f}\right)^2 \left[\frac{\mathrm{SNR}_S}{2\varepsilon \mathrm{SNR}_\pm} + \frac{1}{(1-2\varepsilon)}\right]^{1/2},\end{aligned} \tag{8}$$

where ε is the fraction of time that the laser is tuned to either $f_S + \Delta f$ or $f_S - \Delta f$ and $(1 - 2\varepsilon)$ is the fraction of time that the laser is tuned to f_S. The signal-to-noise ratios at the three frequencies are given by

$$\begin{aligned}\mathrm{SNR}_S &= \frac{N_S{}^2(z, f_S)}{N_S(z, f_S) + N_B(f_S)}, \\ \mathrm{SNR}_+ &= \frac{N_S{}^2(z, f_S + \Delta f)}{N_S(z, f_S + \Delta f) + N_B(f_S + \Delta f)}, \\ \mathrm{SNR}_- &= \frac{N_S{}^2(z, f_S - \Delta f)}{N_S(z, f_S - \Delta f) + N_B(f_S - \Delta f)},\end{aligned} \tag{9}$$

and N_B is the background noise count. In Eqs. (9) we have neglected the small noise terms contributed by photon-count fluctuations in the strong Rayleigh normalizing signals.

To facilitate comparisons with other lidar systems we compute the signal-to-noise ratios by assuming that the laser is tuned all the time to each of the frequencies. The factor ε in Eq. (8) accounts for the different dwell time at each frequency. Because the receiver is not tuned, the mean background count is same for each frequency. At night the background count is negligible compared with the signal count, so the signal-to-noise ratios are equal to the signal counts. We also assume that the Doppler shift associated with radial winds is small, so the signal counts are approximately the same for the two offset frequencies, $f_S \pm \Delta f$. Because the signals are weaker when the laser is tuned to the wing frequencies, collecting data longer at these frequencies reduces the temperature error. The optimum dwell time factor that minimizes the temperature error is given by

$$\varepsilon_{\mathrm{opt}} = \frac{1}{2[1 + (\mathrm{SNR}_\pm/\mathrm{SNR}_S)^{1/2}]} < 0.5. \tag{10}$$

In this case the error is given by

$$\begin{aligned}\Delta T_{\mathrm{rms}}|_{3-\mathrm{freq}} &= \frac{T}{\sqrt{\mathrm{SNR}_S}} 2\left(\frac{\sigma_\lambda}{\Delta f}\right)^2 [1 + (\mathrm{SNR}_S/\mathrm{SNR}_\pm)^{1/2}] \\ &= \frac{T}{\sqrt{\mathrm{SNR}_S}} G_{3f}(\alpha, \beta), \\ G_{3f}(\alpha, \beta) &= \frac{2}{\alpha}\left(1 + \exp(\alpha/4)\left\{\frac{[\exp(\alpha/2) + \beta]}{(1+\beta)}\right\}^{1/2}\right),\end{aligned} \tag{11}$$

where

$$\begin{aligned}\alpha &= \Delta f^2/\sigma_\lambda{}^2, \\ \beta &= N_S(f_S)/N_B.\end{aligned} \tag{12}$$

The temperature error also depends on the offset frequency. Whereas the measurements are more sensitive to temperature for larger offset frequencies, the wing signals are weaker and hence the signal-to-noise ratios are smaller. One can partially compensate for this effect by increasing the dwell time for the wing frequency measurements [inequality (10)]. The optimum choice of offset frequency depends on β, the ratio of the signal to background noise levels. At night $\beta \gg 1$, so $\alpha_{\mathrm{opt}} = 5.114$, $\Delta f_{\mathrm{opt}} = 2.261\sigma_\lambda$, $G_{3f} = 1.796$, $\varepsilon_{\mathrm{opt}} = 0.391$, and $N_S(f_S \pm \Delta f)/N_S(f_S) = 0.0775$. In the daytime $\beta \ll 1$, so $\alpha_{\mathrm{opt}} = 2.557$, $\Delta f_{\mathrm{opt}} = 1.599\sigma_\lambda$, $G_{3f} = 3.591$, $\varepsilon_{\mathrm{opt}} = 0.391$, and $N_S(f_S \pm \Delta f)/N_S(f_S) = 0.2785$. At $T = 200$ K the temperature errors for the optimized systems are

$$\begin{aligned}\Delta T_{\mathrm{rms}}|_{3-\mathrm{freq/night}} &\approx \frac{1.796T}{\sqrt{\mathrm{SNR}_S}} = \frac{359\ \mathrm{K}}{\sqrt{\mathrm{SNR}_S}}, \\ &\qquad \beta \gg 1, \quad \varepsilon_{\mathrm{opt}} = 0.391, \\ \Delta T_{\mathrm{rms}}|_{3-\mathrm{freq/day}} &\approx \frac{3.591T}{\sqrt{\mathrm{SNR}_S}} = \frac{718\ \mathrm{K}}{\sqrt{\mathrm{SNR}_S}} \\ &\qquad \beta \ll 1, \quad \varepsilon_{\mathrm{opt}} = 0.391.\end{aligned} \tag{13}$$

For nighttime measurements, the optimized three-frequency technique has an error that is only 27% larger than the theoretical minimum given by relations (3). Equivalently, to achieve the same performance as the theoretical minimum, the optimized three-frequency technique requires a 2-dB higher signal-to-noise ratio.

Systems that employ AO modulators to shift the frequency of the local oscillator laser are typically designed to operate at a single offset frequency. If the system is optimized for daytime observations

($\Delta f = 1.599\sigma_\lambda$), the nighttime value of G_{3f} is 2.264 and the temperature error is

$$\Delta T_{\mathrm{rms}}|_{3-\mathrm{freq/night}} \approx \frac{2.264T}{\sqrt{\mathrm{SNR}_S}} = \frac{453\ \mathrm{K}}{\sqrt{\mathrm{SNR}_S}}, \quad \beta \gg 1, \quad \varepsilon_{\mathrm{opt}} = 0.327. \quad (14)$$

This suboptimum three-frequency design performs within 4.1 dB of the theoretical minimum at night. In contrast, the daytime error for a system optimized for nighttime observations ($\Delta f = 1.599\sigma_\lambda$) is

$$\Delta T_{\mathrm{rms}}|_{3-\mathrm{freq/day}} \approx \frac{5.435T}{\sqrt{\mathrm{SNR}_S}} = \frac{1090\ \mathrm{K}}{\sqrt{\mathrm{SNR}_S}}, \quad \beta \ll 1, \quad \varepsilon_{\mathrm{opt}} = 0.464. \quad (15)$$

Because the wing signals are less than 8% of the signal at the line peak for this design, the laser must be tuned to the wing frequencies almost 93% of the time to minimize the temperature error.

For the Fe Boltzmann lidar the temperature error is given by[9]

$$\Delta T_{\mathrm{rms}}|_{\mathrm{Fe-Boltz}} \approx \frac{T}{\sqrt{\mathrm{SNR}_{372}}} \times G_B(T,\ \mathrm{SNR}_{372}/\mathrm{SNR}_{374}),$$
$$G_B(T,\ \mathrm{SNR}_{372}/\mathrm{SNR}_{374}) = \frac{T}{598.44K}\left(1 + \frac{\mathrm{SNR}_{372}}{\mathrm{SNR}_{374}}\right)^{1/2}. \quad (16)$$

The value of G_B and hence the error performance of the Boltzmann system is dominated by the signal-to-noise ratio on the weaker 374-nm channel. At night, when the background noise is negligible, $G_B = 1.854$. In the daytime, when the background noise is considerably larger than signal photon noise, $G_B = 9.956$. At $T = 200$ K the temperature errors for the Boltzmann system are given by

$$\Delta T_{\mathrm{rms}}|_{\mathrm{Fe-Boltz/night}} \approx \frac{1.854T}{\sqrt{\mathrm{SNR}_{372}}} = \frac{371\ \mathrm{K}}{\sqrt{\mathrm{SNR}_{372}}}, \quad \beta \gg 1,$$
$$\Delta T_{\mathrm{rms}}|_{\mathrm{Fe-Boltz/day}} \approx \frac{9.956T}{\sqrt{\mathrm{SNR}_{372}}} = \frac{1990\ \mathrm{K}}{\sqrt{\mathrm{SNR}_{372}}}, \quad \beta \ll 1. \quad (17)$$

At night the performances of the Boltzmann and the narrowband three-frequency Fe systems are comparable. During the daytime the three-frequency system has an 8.9-dB performance advantage. The temperature error is 2.77 times smaller than the Boltzmann system for the same signal-to-noise ratio on the 372-nm channels. A practical Boltzmann lidar has the additional disadvantage of requiring two lasers and two telescope systems. In fact, to make the fairest comparison with the three-frequency technique, one should increase the errors listed in relations (17) by $\sqrt{2}$ to reflect the fact that for the Boltzmann technique half of the total laser power is used to probe the 372-nm Fe resonance line and half is used to probe the 374-nm line.

The lidar group at the Institute for Atmospheric Physics, Kuhlungsborn, Germany, employs a frequency-scanning technique for its K lidar that involves measuring the backscattered signal at numerous frequencies within the fluorescence spectrum.[10] A model spectrum is then fitted to the normalized signals so the temperature can be determined. This approach is technically more complex because the frequency of each laser pulse must be measured precisely and the detected signal accumulated as a function of the transmitted frequency. Because multiple frequencies are employed rather than measurements restricted to the most temperature-sensitive region of the spectrum, the error performance is a few decibels worse than that of the three-frequency technique at night and more than 10 dB worse during the day, depending on the range of the frequency scan [see Appendix A, relations (A10)–(A12)]. Even so, this instrument is robust and produces excellent temperature profiles throughout the mesopause region.

An entirely different approach is used to measure temperatures with a Rayleigh lidar. Rayleigh lidars measure the molecular scattered signal from which the relative atmospheric density profile is derived. To determine temperature, one integrates the relative density profile downward from a known or an assumed upper-level temperature, using the hydrostatic equation

$$\mathrm{d}P = -\rho_A g\,\mathrm{d}z \quad (18)$$

and the ideal gas law

$$P = \rho_A RT/M. \quad (19)$$

By combining these two equations and integrating downward one obtains

$$T(z) = \frac{T(z_0)\rho_A(z_0)}{\rho_A(z)} + \frac{M}{R}\int_z^{z_0} \frac{g(r)\rho_A(r)}{\rho_A(z)}\,\mathrm{d}r, \quad (20)$$

where z is the altitude, $T(z)$ is the atmospheric temperature profile [K], $P(z)$ is the atmospheric pressure profile [mbars (1 mb = 100 kPa)], $\rho_A(z)$ is the atmospheric density profile [m^{-3}], M is the mean molecular weight of the atmosphere (28.9644 kg/kmol), R is the universal gas constant (8314.38 J/kmol/K), and z_0 is the altitude of the upper-level temperature estimate [m].

The accuracy of the derived temperatures depends on the signal and background noise levels and on the accuracy of the upper-level temperature estimate. The temperature error is given by[26]

$$\Delta T_{\mathrm{rms}}^2(z)|_{\mathrm{Rayleigh}} \approx \frac{T^2(z)}{\mathrm{SNR}_R(z)} + \frac{\rho_A^2(z_0)}{\rho_A^2(z)} \times \left[\Delta T^2(z_0) + \frac{T^2(z_0)}{\mathrm{SNR}_R(z_0)}\right] \quad (21)$$

Table 3. System Parameters and Temperature Errors for Middle-Atmosphere Lidars at $T = 200$ K

Type of System	Δf	$N_S(f_S \pm \Delta f)/N_S(f_S)$	ε_{opt}	ΔT_{rms}
Three-frequency narrowband (Na, Fe, K, Ca, and Ca^+)[a]				
Day at optimum day configuration	$1.599\sigma_\lambda$	0.2785	0.391	$\frac{3.591T}{\sqrt{SNR_S}} \approx \frac{718\text{ K}}{\sqrt{SNR_S}}$
Day at optimum night configuration	$2.261\sigma_\lambda$	0.0775	0.464	$\frac{5.435T}{\sqrt{SNR_S}} \approx \frac{1090\text{ K}}{\sqrt{SNR_S}}$
Night at optimum night configuration	$2.261\sigma_\lambda$	0.0775	0.391	$\frac{1.796T}{\sqrt{SNR_S}} \approx \frac{359\text{ K}}{\sqrt{SNR_S}}$
Night at optimum day configuration	$1.599\sigma_\lambda$	0.2785	0.327	$\frac{2.264T}{\sqrt{SNR_S}} \approx \frac{453\text{ K}}{\sqrt{SNR_S}}$
	Δf_{scan}	$N_S(f_S \pm \Delta f_{scan}/2)/N_S(f_S)$		
Frequency-scanning narrowband Na, Fe, K, Ca, and Ca^+[b]				
Day	$6\sigma_\lambda$	0.011	NA[c]	$\frac{16.02T}{\sqrt{SNR_S}} \approx \frac{3200\text{ K}}{\sqrt{SNR_S}}$
Night	$6\sigma_\lambda$	0.011	NA	$\frac{2.188T}{\sqrt{SNR_S}} \approx \frac{438\text{ K}}{\sqrt{SNR_S}}$
Night theoretical minimum[d]	NA	NA	NA	$\frac{\sqrt{2}T}{\sqrt{SNR_S}} \approx \frac{283\text{ K}}{\sqrt{SNR_S}}$
Fe Boltzmann broadband[e]				
Day	NA	NA	NA	$\frac{9.856T}{\sqrt{SNR_{372}}} \approx \frac{1990\text{ K}}{\sqrt{SNR_{372}}}$
Night	NA	NA	NA	$\frac{1.854T}{\sqrt{SNR_{372}}} \approx \frac{371\text{ K}}{\sqrt{SNR_{372}}}$
Rayleigh day or night	NA	NA	NA	$\frac{T}{\sqrt{SNR_R}} \approx \frac{200\text{ K}}{\sqrt{SNR_R}}$

[a] Three-frequency laser technique.
[b] Relations (A11) and (A12) of Appendix A with $\alpha_{scan} = 6$ and $\Delta f_{scan} = 6\sigma_D \approx 6\sigma_\lambda$.
[c] Not applicable.
[d] Infinite spectral resolution receiver technique.
[e] Assuming equal laser power at 372 and 374 nm and that total laser power is double that for the three-frequency technique.

for both daytime and nighttime measurements, where SNR_R is the signal-to-noise ratio for the molecular or Rayleigh backscattered signal:

$$SNR_R(z) = \frac{N_R^2(z, \lambda)}{N_R(z, \lambda) + N_B(\lambda)}. \tag{22}$$

For altitudes ~1.5 scale heights (~10 km) or more below z_0, the derived temperature is insensitive to the upper-level temperature estimate, so the temperature error reduces to

$$\Delta T_{rms}|_{Rayleigh} \approx T/\sqrt{SNR_R}. \tag{23}$$

Notice that the Rayleigh technique performs 3 dB better than the theoretical minimum for lidars that measure the spectral width of the backscattered signal [relations (3)]. Rayleigh lidars do not measure the true kinetic temperature of the atmosphere. Their apparent performance advantage arises because the data are processed under the assumption that the atmosphere is in hydrostatic equilibrium such that Eqs. (18) and (19) are valid. This is a reasonable assumption for the middle atmosphere.

Because resonance fluorescence lidars also measure the molecular scattered signal below the mesospheric metal layers, one can process these data to determine temperatures at lower altitudes by using the Rayleigh inversion algorithm. If the molecular signal-to-noise ratio is sufficiently large near the bottom edge of the metal layer, then the temperature derived from the resonance fluorescence lidar at the bottom of the metal layer can be used as the initial estimate in the Rayleigh retrieval.[13] In this case it would be feasible to derive nearly continuous temperature profiles extending from the lower stratosphere through the metal layer into the lower thermosphere.

The error performances of the middle-atmosphere temperature lidars are summarized in Table 3 and plotted in Fig. 3 as a function of signal-to-noise ratio. Notice the curves that correspond to the three-frequency technique optimized for daytime observations. This system has the widest range of applicability because it provides good accuracies during both day and night. To achieve an accuracy of ± 1 K with this technique requires signal-to-noise ratios of 5.2×10^5 during the day and 2.1×10^5 at night. By comparison, the Rayleigh lidar requires a signal-to-noise ratio of just 4×10^4 during either day or night. However, at the height of the metal layers, fluorescence scattering from Na, Fe, K, Ca, and Ca^+

is typically many orders of magnitude stronger than molecular scattering. At these highest altitudes the fluorescence lidars outperform the Rayleigh lidars by a significant margin.

4. Error Analysis for Wind Measurements

The narrowband fluorescence lidars can also measure the wind velocity, provided that the laser can be locked to the peak of the resonance line or the tuning error can be estimated, say, by averaging of the measured vertical winds over the species layer to yield the velocity bias. The wind metric is the ratio of the Rayleigh normalized wing signals:

$$R_V = \frac{N_S(f_S - \Delta f)}{N_S(f_S + \Delta f)} = \exp\left(\frac{2\Delta f}{\lambda_S \sigma_\lambda^{\,2}} V_R\right). \qquad (24)$$

The radial velocity is given by

$$V_R = \frac{\lambda_S \Delta f}{2} \frac{\ln(R_V)}{\ln(R_T)} = \frac{\lambda_S \Delta f}{2} \frac{\ln\left[\dfrac{N_S(f_S - \Delta f)}{N_S(f_0 + \Delta f)}\right]}{\ln\left[\dfrac{N_S^{\,2}(f_S)}{N_S(f_S + \Delta f) N_S(f_S - \Delta f)}\right]}. \qquad (25)$$

The rms velocity error is given by

$$\Delta V_{\mathrm{rms}}|_{3-\mathrm{freq}} = \left(\frac{\sigma_\lambda}{\Delta f}\right)^2 \left\{\frac{2}{\varepsilon \mathrm{SNR}_\pm}\left[\left(\frac{\lambda_S \Delta f}{2}\right)^2 + V^2\right] + \frac{4}{(1 - 2\varepsilon)\mathrm{SNR}_S} V^2\right\}^{1/2} \approx \frac{\lambda_S \Delta f}{\sqrt{\mathrm{SNR}_S}} \left(\frac{\sigma_\lambda}{\Delta f}\right)^2 [(\mathrm{SNR}_S/\mathrm{SNR}_\pm)^{1/2} + \mathrm{SNR}_S/\mathrm{SNR}_\pm]^{1/2}. \qquad (26)$$

For a system that is optimized for daytime temperature measurements and assuming that $\sigma_L \ll \sigma_D$, relation (26) reduces to

$$\Delta V_{\mathrm{rms}}|_{3-\mathrm{freq/night}} \approx \frac{1.465 \lambda_S \sigma_D}{\sqrt{\mathrm{SNR}_S}} = \frac{253 \text{ m/s}}{\sqrt{\mathrm{SNR}_S}}, \quad \beta \gg 1,$$

$$\Delta V_{\mathrm{rms}}|_{3-\mathrm{freq/day}} \approx \frac{2.539 \lambda_S \sigma_D}{\sqrt{\mathrm{SNR}_S}} = \frac{438 \text{ m/s}}{\sqrt{\mathrm{SNR}_S}} \quad \beta \ll 1. \qquad (27)$$

The right-hand-sides of relations (27) correspond to the three-frequency Fe lidar.

If the offset frequency is chosen to minimize the wind error and if the dwell time factor is chosen to minimize the temperature error, then $\Delta f_{\mathrm{opt}} = 1.558\sigma_\lambda$ for nighttime measurements and $\Delta f_{\mathrm{opt}} = 1.102\sigma_\lambda$ for daytime measurements. Fortunately, a system that is optimized for daytime temperature measurements ($\Delta f_{\mathrm{opt}} = 1.599\sigma_\lambda$) will perform close to the optimum for nighttime wind measurements and provide good wind measurements during the day, as is illustrated in Table 4, where the key system parameters and the temperature and winds errors are listed for both day and night observations when the three-frequency Fe lidar is optimized for either temperature or wind observations. Optimizing the system for daytime temperature measurements (both offset frequency and dwell time factor) appears to be a good compromise that yields low measurement errors for both temperature and winds during day and night. Choosing another optimization compromises at least one of the measurements, especially during the day.

The velocity errors for the metal species are summarized in Table 5 and plotted in Fig. 4 versus signal-to-noise ratio for systems that are optimized for daytime temperature measurements. Because Fe is the most massive species, the three-frequency Fe lidar achieves the best performance for a given signal-to-noise ratio, although the advantage is not large.

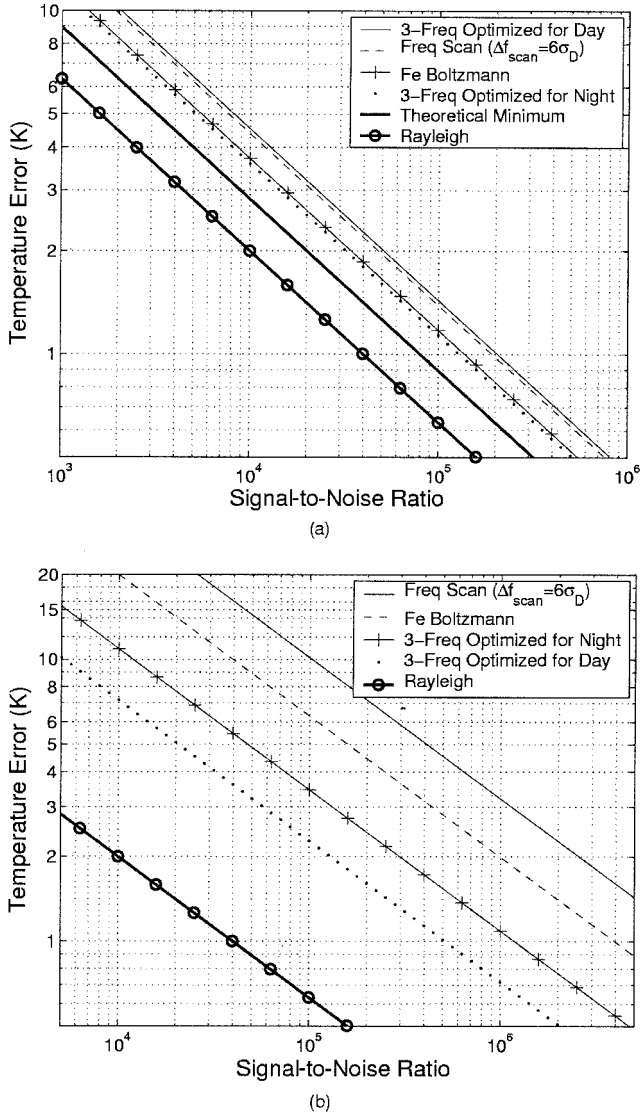

Fig. 3. Rms temperature error plotted versus signal-to-noise ratio for various resonance fluorescence and Rayleigh lidar system configurations: (a) nighttime measurements, (b) daytime measurements.

Table 4. Temperature and Wind Errors for Three-Frequency Fe Lidars at $T = 200$ K

Condition	Δf_{opt} (MHz)	ε_{opt}	ΔT_{rms}	ΔV_{rms}
Optimized for Temperature Observations				
Day at optimum day configuration	742	0.391	$\frac{718\ \text{K}}{\sqrt{\text{SNR}_{\text{Fe}}}}$	$\frac{438\ m/s}{\sqrt{\text{SNR}_{\text{Fe}}}}$
Day at optimum night configuration	1049	0.464	$\frac{1090\ \text{K}}{\sqrt{\text{SNR}_{\text{Fe}}}}$	$\frac{1021\ m/s}{\sqrt{\text{SNR}_{\text{Fe}}}}$
Night at optimum night configuration	1049	0.391	$\frac{359\ \text{K}}{\sqrt{\text{SNR}_{\text{Fe}}}}$	$\frac{310\ \text{m/s}}{\sqrt{\text{SNR}_{\text{Fe}}}}$
Night at optimum day configuration	742	0.327	$\frac{453\ \text{K}}{\sqrt{\text{SNR}_{\text{Fe}}}}$	$\frac{253\ \text{m/s}}{\sqrt{\text{SNR}_{\text{Fe}}}}$
Optimized for wind observations				
Day at optimum day configuration	511	0.324	$\frac{934\ \text{K}}{\sqrt{\text{SNR}_{\text{Fe}}}}$	$\frac{357\ \text{m/s}}{\sqrt{\text{SNR}_{\text{Fe}}}}$
Day at optimum night configuration	723	0.386	$\frac{719\ \text{K}}{\sqrt{\text{SNR}_{\text{Fe}}}}$	$\frac{425\ \text{m/s}}{\sqrt{\text{SNR}_{\text{Fe}}}}$
Night at optimum night configuration	723	0.324	$\frac{467\ \text{K}}{\sqrt{\text{SNR}_{\text{Fe}}}}$	$\frac{253\ \text{m/s}}{\sqrt{\text{SNR}_{\text{Fe}}}}$
Night at optimum day configuration	511	0.288	$\frac{776\ \text{K}}{\sqrt{\text{SNR}_{\text{Fe}}}}$	$\frac{280\ \text{m/s}}{\sqrt{\text{SNR}_{\text{Fe}}}}$
Night theoretical minimum[a]	NA[b]	NA	$\frac{283\ \text{K}}{\sqrt{\text{SNR}_{\text{Fe}}}}$	$\frac{173\ \text{m/s}}{\sqrt{\text{SNR}_{\text{Fe}}}}$

[a]Infinite spectral resolution receiver technique.
[b]Not applicable.

To achieve an accuracy of ± 1 m/s with an Fe system requires a signal-to-noise ratio of 1.9×10^5 during the day and 6.4×10^4 at night. At night this system performs within 1.7 dB of the theoretical minimum for fluorescence lidars given by relations (3). By comparison, the Na lidar requires signal-to-noise ratios of 4.7×10^5 during the day and 1.6×10^5 at night. However, as we shall see in the Section 5, for equal laser powers and telescope aperture areas, SNR_{Na} is many times larger than SNR_{Fe}.

5. Signal-to-Noise Ratios

The theoretical performance of any lidar system is governed by the lidar equation. The expected signal photon count is equal to the product of the system efficiency, the number of photons transmitted by the laser, the probability that a transmitted photon is scattered, and the probability that a scattered photon is detected. For narrowband fluorescence systems for which $\sigma_L \ll \sigma_D$, the lidar equation is given approximately by[26]

$$N_S(z) = (\eta T_A^2)\left(\frac{P_L \tau}{hc/\lambda_S}\right)[\sigma_S \rho_S(z)\Delta z]\left(\frac{A_T}{4\pi z^2}\right), \quad (28)$$

where $N_S(z)$ is the expected number of photons detected in range interval $(z - \Delta z/2, z + \Delta z/2)$, η is the lidar system efficiency including detector quantum efficiency, T_A^2 is the two-way atmospheric transmit-

Table 5. Velocity Errors for Three-Frequency Systems Optimized for Daytime Temperature Measurements at $T = 200$ K

Species	Offset Frequency, Δf (MHz)	Daytime ΔV_{rms}	Nighttime ΔV_{rms}
Na	730	$\frac{683\ \text{m/s}}{\sqrt{\text{SNR}_{\text{Na}}}}$	$\frac{394\ \text{m/s}}{\sqrt{\text{SNR}_{\text{Na}}}}$
Fe	742	$\frac{438\ \text{m/s}}{\sqrt{\text{SNR}_{\text{Fe}}}}$	$\frac{253\ \text{m/s}}{\sqrt{\text{SNR}_{\text{Fe}}}}$
K	428	$\frac{524\ \text{m/s}}{\sqrt{\text{SNR}_{\text{K}}}}$	$\frac{302\ \text{m/s}}{\sqrt{\text{SNR}_{\text{K}}}}$
Ca	771	$\frac{517\ \text{m/s}}{\sqrt{\text{SNR}_{\text{Ca}}}}$	$\frac{298\ \text{m/s}}{\sqrt{\text{SNR}_{\text{Ca}}}}$
Ca^+	828	$\frac{517\ \text{m/s}}{\sqrt{\text{SNR}_{\text{Ca}^+}}}$	$\frac{298\ \text{m/s}}{\sqrt{\text{SNR}_{\text{Ca}^+}}}$

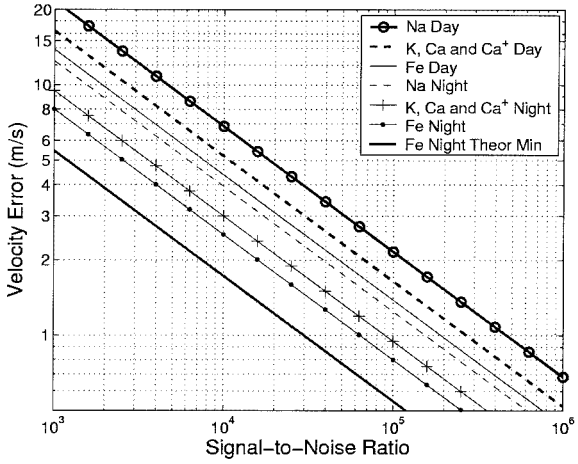

Fig. 4. Rms radial velocity error plotted versus signal-to-noise ratio for various resonance fluorescence lidar system configurations: three-frequency wind measurements.

Table 6. Measured Na Layer Parameters

Parameter	Measured by Plane *et al.*[a]	Measured by States and Gardner[b]	Mean
Centroid height (km)	91.6	91.4	91.5
Rms width (km)	4.38	4.91	4.6
Abundance ($\times 10^9$ cm^{-2})	4.26	3.71	4.0

[a]Ref. 27.
[b]Ref. 28.

tance at species resonance wavelength, P_L is the average laser power [W], τ is the measurement integration time [s], h is Planck's constant (6.63×10^{-34} J/s), c is the velocity of light (3×10^8 m/s), σ_S is the peak scattering cross section of the species [m^2], $\rho_S(z)$ is the species density at range z [m^{-3}], Δz is the range bin length [m], and A_T is the receiving telescope's aperture area [m^2].

The metal layers vary in density, height, and width. The most convenient way to compare system performance is to compute the signal-to-noise ratio by using the expected total signal. The total signal is obtained by integrating Eq. (28) over the whole layer. At night when background noise is negligible, the signal-to-noise ratio is equal to the total signal count and is given by

$$(\mathrm{SNR}_S)_{\mathrm{Night}} = \left(\frac{\eta P_L A_T \tau}{4\pi hc}\right)\left[\frac{T_A^{\,2}(\lambda_S)}{z_S^{\,2}}\,\lambda_S \sigma_S C_S\right], \quad (29)$$

where z_S [m] is the centroid height of the metal layer and C_S [m^{-2}] is the column abundance.

In Eq. (29) the signal-to-noise ratio has been expressed as the product of a term that depends on lidar engineering factors such as system efficiency, laser power, and telescope aperture area and another term that depends natural factors such as laser wavelength, atmospheric transmittance, species cross section, and species abundance. Tables 6–10 summarize the measured parameters of the mesospheric Na, Fe, K, Ca, and Ca^+ layers. Table 11 lists the two-way atmospheric transmittance at each resonance wavelength for zenith observations at sea level. The values correspond to a clear atmosphere where aerosol attenuation is negligible. They were derived from the LOWTRAN atmospheric transmission code developed by the U.S. Air Force.[38] To compare the performances of the different fluorescence lidars, we assume that the lidar engineering factors are identical for each lidar. The nighttime signal-to-noise ratio was computed for each species from Eq. (29) and was normalized to the value for Na:

$$(\mathrm{SNR}_S/\mathrm{SNR}_{\mathrm{Na}})_{\mathrm{Night}} \approx \left[\frac{T_A^{\,2}(\lambda_S)}{z_S^{\,2}}\,\lambda_S \sigma_S C_S\right] \Bigg/ \left[\frac{T_A^{\,2}(\lambda_{\mathrm{Na}})}{z_{\mathrm{Na}}^{\,2}}\,\lambda_{\mathrm{Na}} \sigma_{\mathrm{Na}} C_{\mathrm{Na}}\right]. \quad (30)$$

The results are tabulated in Table 12. Na has a significant advantage (12.5 dB or more) over the other species. Even so, Fe and K systems have provided excellent low time-resolution data, which are important for characterizing the background temperature structure of the mesopause region.

The expected photon count from molecular scattering is also given by Eq. (29) but with the species cross section replaced by Rayleigh backscatter cross section σ_R and the species density replaced by atmospheric density $\rho_A(z)$:

$$N_R(z) = (\eta T_A^{\,2})\left(\frac{P_L \tau}{hc/\lambda}\right)[\sigma_R \rho_A(z) \Delta z]\left(\frac{A_T}{4\pi z^2}\right). \quad (31)$$

The product of the Rayleigh cross section and the atmospheric density can be expressed in terms of the atmospheric pressure [$P(z)$, in millibars] and temperature and the laser wavelength[9]:

$$\sigma_R(\lambda)\rho_A(z) = 3.692 \times 10^{-31}\,\frac{P(z)}{T(z)}\,\frac{1}{\lambda^{4.0117}}. \quad (32)$$

Assuming that the lidar engineering factors are identical and that background noise is negligible at night, the ratio of SNR_R at a given altitude for an arbitrary laser wavelength to the value for the commonly used frequency-doubled Nd:YAG laser operating at 532.070 nm is

$$(\mathrm{SNR}_\lambda/\mathrm{SNR}_{532})_{\mathrm{Night}} = \frac{T_A^{\,2}(\lambda)}{T_A^{\,2}(\lambda_{532})}\left(\frac{\lambda_{532}}{\lambda}\right)^{3.0117}. \quad (33)$$

The relative Rayleigh signal-to-noise ratios for nighttime observations are tabulated in Table 12. As expected, systems that employ the shorter wavelengths have the advantage. Among the fluorescence lidars, Fe, Ca, and Ca^+ achieve the best performance when they are used to make nighttime Rayleigh temperature measurements.

Background noise from scattered sunlight has a significant effect on measurement accuracy during

Table 7. Measured Fe Layer Parameters

Parameter	Measured by Kane and Gardner[a]	Measured by Raizada and Tepley[b]	Mean
Centroid height (km)	88.1	88.5	88.3
Rms width (km)	3.41	5.49	4.5
Abundance ($\times 10^9$ cm^{-2})	10.63	9.73	10.2

[a]Ref. 29.
[b]Ref. 30.

Table 8. Measured K Layer Parameters

Parameter	Measured by Eska *et al.*[a]	Measured by Friedman *et al.*[b]	Mean
Centroid height (km)	90.5	91.5	91.0
Rms width (km)	4.0	5.4	4.7
Abundance ($\times 10^7$ cm^{-2})	4.4	4.5	4.5

[a]Ref. 31.
[b]Ref. 32.

Table 9. Measured Ca Layer Parameters

Parameter	Measured by Granier *et al.*[a]	Measured by Qian and Gardner[b]	Measured by Alpers *et al.*[c]	Measured by Gerding *et al.*[d]	Mean
Centroid Height (km)	89.2	91.8			90.5
Rms width (km)	4.7	3.5	1.8	4.0	3.5
Abundance ($\times 10^7$ cm^{-2})	2.7	6.3	2.2	2.4	3.4

[a]Ref. 33.
[b]Ref. 34.
[c]Ref. 35.
[d]Ref. 36.

daytime. The expected background photon count per range bin is given by

$$N_B(\lambda) = \eta_T \frac{S_{\mathrm{Sky}}(\lambda) A_T \Delta\lambda \Omega_{\mathrm{FOV}} (2\Delta z/c)}{hc/\lambda} r_L \tau, \quad (34)$$

where η_T is the optical efficiency of the telescope including detector quantum efficiency, $S_{\mathrm{Sky}}(\lambda)$ is the sky's spectral radiance [W/m^2/nm/sr], $\Delta\lambda$ is the optical bandwidth of the receiving telescope [nm], Ω_{FOV} is the solid-angle field of view of the receiving telescope [sr], and r_L is the laser pulse rate [s^{-1}].

The sky's spectral radiance depends on many factors, including the elevation angle of the Sun, the pointing direction of the lidar relative to the Sun, the altitude of the lidar, and the laser wavelength. Whereas the spectral distribution of solar radiation approximates a blackbody at 5900 K, absorption by atomic constituents in the outer atmosphere of the Sun (Fraunhofer lines) and by molecular constituents in the Earth's atmosphere has a significant influence on the sky's spectral radiance. For the purpose of comparing the daytime performances of the various lidars, we need only to determine the relative sky brightness at the key laser wavelengths.

Mercherikunnel and Duncan[39] tabulated the direct solar spectral irradiance [W/m^2/nm] observed at Table Mountain, Calif., at 300–3000-nm wavelength. The resolution of their instruments was not sufficient to permit them to observe the solar Fraunhofer lines, but the data do provide a good characterization of the solar continuum observed at ground level. The Mercherikunnel–Duncan observations were scaled to the sky's radiance spectrum at 500 nm (0.90 W/m^2/nm/sr) published by Pratt[40] for zenith observations at sea level under conditions of excellent visibility with the Sun at an elevation of 45°. The results are tabulated in Table 11 for the key laser wavelengths.

Also tabulated in Table 11 are the spectral widths and relative depths of the solar Fraunhofer lines ob-

Table 10. Measured Ca$^+$ Layer Parameters

Parameter	Granier *et al.*[a]	Gardner *et al.*[b]	Alpers *et al.*[c]	Gerding *et al.*[d]	Mean
Centroid Height (km)	93.7	96.8	97.6	91.9	95.0
Rms width (km)	5.1		3.4	2.3	3.6
Abundance ($\times 10^7$ cm^{-2})	2.1	6.9	14.8	4.9	7.2

[a]Ref. 33.
[b]Ref. 37.
[c]Ref. 35.
[d]Ref. 36.

Table 11. Atmospheric Parameters

Species or Laser	λ_S (nm)	Two-way Atmospheric Transmittance, T_A^2	Sky Spectral Radiance Continuum ($\times 10^{-3}$ W/m^2/nm/sr)[a]	Fraunhofer Line Relative Depth (% Continuum)[b]	Fraunhofer Linewidth (GHz)[c]	Narrowband Sky Spectral Radiance ($\times 10^{-3}$ W/m^2/nm/sr)[a,d]
Na	588.995	0.49	86.3	9.6	14.5	8.28
Fe	371.994	0.25	34.8	8.1	36.0	2.82
K	769.896	0.64	67.7	21.7	5.9	14.69
Ca	422.673	0.37	67.7	7.6	23.2	5.15
Ca$^+$	393.366	0.30	41.0	9.9	554.0	4.06
Frequency-doubled Nd:YAG	532.070	0.46	90.0	NA[e]	NA	90.0
Frequency-tripled Nd:YAG	354.713	0.23	27.9	NA	NA	27.9

[a]Zenith viewing at sea level, solar zenith angle 45°, excellent visibility.
[b]Includes 5% Ring effect for all lines.
[c]Full width at twice depth.
[d]Receiver bandwidth much smaller than Fraunhofer linewidth.
[e]Not applicable.

Table 12. Relative Nighttime Signal-to-Noise Ratios

Species or Laser	Wavelength (nm)	Fluorescence SNR_S/SNR_{Na} (db)	Rayleigh SNR_λ/SNR_{532} (db)
Na	588.995	0	−1.1
Fe	371.994	−12.5	+2.0
K	769.896	−17.6	−3.4
Ca	422.673	−19.1	+2.1
Ca^+	393.366	−21.9	+2.1
Frequency-doubled Nd:YAG	532.070	NA[a]	0
Frequency-tripled Nd:YAG	354.713	NA	+2.3

[a]Not applicable.

served in the diffuse component of atmospheric scattered sunlight that correspond to the Na, Fe, K, Ca, and Ca^+ resonance lines. The line depths, as a percentage of the continuum, were determined by use of the high-resolution solar spectra measured at Jungfraujoch, Switzerland, by Delbouille *et al.*[41] and are available on the Internet (http://mesola.obspm.fr/). These data were obtained by direct observation of the solar disk. The Fraunhofer lines in the diffuse component of the scattered solar radiation are partially filled in by rotational Raman scattering of the bright continuum by atmospheric O_2 and N_2. This feature is called the Ring effect[42] and is usually characterized as a percent of the continuum. Typical Ring effect intensities vary from 1% to 6% and are dependent on solar zenith angle as well as on surface albedo.[43] Unfortunately, the Ring effect has not been fully characterized for all the metal resonance lines. For this analysis we use a conservative value of 5% for all the Fraunhofer lines associated with the metal resonance wavelengths. This value was added to the line depths derived from the solar spectrum, and the sums are tabulated in Table 11.

The Fraunhofer linewidths were determined by measurement of the full bandwidth at twice the line depth including the Ring effect. These values are listed in Table 11. For the Na, Fe, Ca, and Ca^+ Fraunhofer lines, the full width at twice the line depth is approximately equal to the equivalent rms linewidth that would be obtained by fitting a simple Gaussian absorption line profile to the measured line center radiance and the twice the line depth radiance points. For K, the equivalent rms linewidth is approximately 62% of the value listed. If the optical bandwidth of the receiving telescope is much less than the Fraunhofer linewidth, the sky's spectral radiance is the product of the radiance continuum listed in Table 11 and the depth of the corresponding Fraunhofer line. The values of sky spectral radiance for such a narrowband receiver are listed in column 7 of Table 11.

The signal-to-noise ratios for daytime operation when the background noise count is significantly larger than the signal count are given by

$$(SNR_S)_{Day} \approx N_S^2(z, \lambda_S)/N_B(\lambda_S), \quad \text{fluorescence lidars},$$
$$(SNR_R)_{Day} \approx N_R^2(z, \lambda)/N_B(\lambda), \quad \text{Rayleigh lidars}. \tag{35}$$

One computes the relative signal-to-noise ratios by assuming that the engineering factors such as the laser power and pulse rate and the telescope aperture area, field of view, and optical bandwidth are identical for each lidar:

$$(SNR_S/SNR_{Na})_{Day} \approx \frac{\lambda_{Na} S_{Sky}(\lambda_{Na})}{\lambda_S S_{Sky}(\lambda_S)} \times (SNR_S/SNR_{Na})_{Night}^2, \quad \text{fluorescence lidars},$$
$$(SNR_\lambda/SNR_{532})_{Day} \approx \frac{\lambda_{532} S_{Sky}(\lambda_{532})}{\lambda S_{Sky}(\lambda)} \times (SNR_\lambda/SNR_{532})_{Night}^2, \quad \text{Rayleigh lidars}. \tag{36}$$

The results are tabulated in Table 13. They reflect fundamental differences in natural factors such as species abundance, scattering cross section, laser

Table 13. Relative Daytime Signal-to-Noise Ratios

Species or Laser	Wavelength (nm)	Fluorescence SNR_S/SNR_{Na} (db)	Rayleigh SNR_λ/SNR_{532} (db)
Na	588.995	0	+7.8
Fe	371.994	−18.4	+20.7
K	769.896	−38.8	−0.5
Ca	422.673	−34.8	+17.6
Ca^+	393.366	−39.0	+19.0
Frequency-doubled Nd:YAG	532.070	NA[a]	0
Frequency-tripled Nd:YAG	354.713	NA	+11.5

[a]Not applicable.

wavelength, atmospheric transmittance, and sky brightness.

6. Discussion

Among the resonance fluorescence techniques, the Na lidar has the clear performance advantage for both day and night observations. The combination of a large backscatter cross section, relatively large Na abundance, and good atmospheric transmittance yields signal-to-noise ratios that are more than 12 dB larger at night and 18 dB larger during the day than those of any other fluorescence lidar. For applications that require high measurement accuracy and high temporal and spatial resolution, such as the study of gravity wave dynamics and fluxes, Na lidars are the instruments of choice. The technique has been used to study mesospheric instabilities,[7] heat fluxes,[44] atmospheric tides,[11,12] and long-term temperature variations in the mesopause region.[45] Unfortunately, modern Na wind–temperature lidars are complex sensitive instruments that utilize both solid-state and dye laser technology. The instruments require temperature-controlled, low-vibration environments for their operation, and this restriction has precluded their deployment at remote sites and on mobile platforms such as aircraft and ships.

The K temperature lidar was developed by use of a more rugged, injection-seeded alexandrite laser technology.[10] Although the abundance of K is 2 orders of magnitude smaller than that of Na, K systems have been used to make important observations of the background temperature structure of the mesopause region at several sites,[46,47] including Svalbard (78 °N) in the Norwegian Arctic.[48] However, long integration periods, especially during the day, are required for scientifically useful temperature data to be produced. As a consequence, these systems are best suited for characterizing the background temperature structure and, perhaps, atmospheric tides.

The three-frequency narrowband Fe lidar has a performance advantage over the K lidar of 5 dB at night and of more than 20 dB during the day. These systems can be developed by use of the same alexandrite laser technologies employed in the K systems. Because the IR output of the alexandrite laser must be frequency doubled to probe the 372-nm (or 386-nm) Fe resonance line, there is an additional loss of ~3 dB associated with the doubling process. In this case the nighttime performances of the K and Fe lidars differ by only a few decibels. Initial tests of this concept were conducted recently with the 386-nm Fe resonance line.[18] This line has a 40% smaller cross section, and the IR fundamental is farther from the peak of the alexandrite gain curve than for the 372-nm line. Consequently, systems based on the 372-nm line would have a 4–5 dB performance advantage.

The performance of the Fe Boltzmann lidar is comparable with that of the three-frequency Fe lidar at night but suffers a 9-dB performance penalty during the day. Although this system has been used to acquire scientifically important data during both day and night and from research aircraft,[13,25] practical systems require two lasers and two receiving systems, which contribute to cost and complexity. Because the robust alexandrite ring laser technology that has been developed for K temperature lidars[10,17] can also be used for Fe, the three-frequency Fe technique appears to have a significant advantage. Fe systems also exhibit superb performance as Rayleigh lidars, especially during the day.[13,49] The short wavelength in the near UV enhances the molecular backscattered signal, and the strong Fraunhofer line significantly reduces the background noise from scattered sunlight during the day. Ca and Ca^+ lidars could be developed to measure middle-atmosphere temperatures by use of a combination of the Rayleigh and three-frequency techniques. However, these systems would have no performance or technology advantages over Fe systems. Because Ca^+ densities are typically small and highly variable, systems based on this species cannot reliably provide the long-term measurements that are required for characterizing tides and the background temperature structure.

The performance comparisons tabulated in Tables 12 and 13 assume that the laser power levels, telescope aperture areas, and system efficiencies are the same for each species. Currently, laser power levels vary from approximately 1 to 2 W for Na systems that employ dye lasers and amplifiers, 5 to 10 W for Fe and K lidars that employ alexandrite lasers, to 10 to 40 W or more for the frequency-doubled and -tripled Nd:YAG lasers employed in modern Rayleigh lidars. Photomultiplier tube quantum efficiencies also vary from ~30% for Fe systems to ~15% for K, although it is possible to use photon-counting avalanche photodiodes, with quantum efficiencies approaching 70%, for some applications in the near IR.[50] Narrowband Faraday filters, with bandwidths that are comparable with the fluorescence linewidth, have been developed for daytime Na and K observations.[50] These filters cannot easily be developed for the other species, so daytime receivers for Fe, Ca, and Ca^+ must employ stabilized Fabry–Perot etalons for rejection of background noise. All these factors influence measurement accuracy and will alter the comparisons of performance among actual systems.

In summary, routine measurements of middle-atmosphere temperature profiles are now possible during the night with a variety of resonance fluorescence and Rayleigh lidar techniques. Rugged instruments have been fielded in research aircraft and deployed to remote sites in both the Arctic and the Antarctic. The three-frequency fluorescence technique utilizes technology that is mature and robust. Well-designed systems are capable of performing within a few decibels of the theoretical limits for both temperature and wind observations. Future developments will focus on extending routine observations into the daytime, simplifying the laser technology, and making it more rugged. Because of their superb performance as Rayleigh lidars, three-frequency Fe systems are likely to receive increasing attention because they have the potential for providing excellent

temperature data during both day and night throughout the middle atmosphere from ~25 to 110 km or more.

Appendix A

For an ideal receiver that measures the precise frequency of each detected photon, the maximum-likelihood estimates of the Doppler shift (V_R/λ) and thermal broadening ($\sigma_D{}^2 = \gamma T$) are the values that maximize the probability of observing the measured photon frequencies. Assume that the ideal receiver detects N photons with frequencies $f_1, f_2, f_3 \ldots f_N$. The photon frequencies are identically distributed independent random variables. In the absence of background noise the probability distribution of the photon frequencies equals the normalized fluorescence spectrum[51]:

$$p(f_i) = \frac{S(f_i)}{\int_0^\infty S(f)\mathrm{d}f} = \frac{\exp[-(f_i - f_S + V_R/\lambda_S)^2/2\sigma_D{}^2]}{\sqrt{2\pi}\sigma_D}, \tag{A1}$$

where $S(f)$ is given by Eq. (1). The probability of observing these frequencies, given V_R and T, is

$$\mathrm{prob}[f_1, f_2, \ldots f_N | V_R, T] = \prod_{i=1}^{N} p(f_i)\mathrm{d}f. \tag{A2}$$

Maximizing Eq. (A2) is equivalent to maximizing the logarithm of Eq. (A2) such that the likelihood function is defined by

$$\begin{aligned} l(V_R, T) &= \sum_{i=1}^{N} \ln p(f_i) \\ &= -N \ln(\sqrt{\gamma T}) - \sum_{i=1}^{N} (f_i - f_S \\ &\quad + V_R/\lambda_S)^2/2\gamma T. \end{aligned} \tag{A3}$$

This likelihood function is maximized when

$$\begin{aligned} V_R &= -\frac{\lambda_S}{N}\sum_{i=1}^{N}(f_i - f_S), \\ T &= \sigma_D{}^2/\gamma = \frac{1}{\gamma N}\sum_{i=1}^{N}(f_i - f_S + V_R/\lambda_S)^2, \end{aligned} \tag{A4}$$

where γ is defined in Eqs. (2). Notice that the velocity is related to the sample mean frequency, whereas the temperature is related to the sample frequency variance. The maximum-likelihood estimators given by Eqs. (A4) are unbiased statistics for velocity and temperature. The mean-square errors depend on the statistical fluctuations in the measured photon frequencies. For a Gaussian line shape the errors are

$$\begin{aligned} \langle \Delta V_R{}^2 \rangle &= \frac{\lambda_S{}^2 \sigma_D{}^2}{N}, \\ \langle \Delta T^2 \rangle &= \frac{2T^2}{N}. \end{aligned} \tag{A5}$$

When the fluorescence line shape is Gaussian, measuring the photon frequencies is equivalent to sampling a Gaussian distributed random variable [Eq. (A1)] to determine the mean and the variance of the distribution. For Gaussian random variables the maximum-likelihood estimates of the mean and the variance of the distribution are also the minimum mean-square-error estimators, so Eqs. (A5) represent the theoretical minimum errors that can be achieved.

Alternatively, a narrowband laser could be scanned over the whole fluorescence line and the backscattered photon counts recorded as a function of the laser frequency. Temperature and wind can be inferred by fitting of a model spectrum to the data.[10] To analyze the error performance of this approach we assume that the laser linewidth is negligible compared with the fluorescence linewidth and that the scanning range $\Delta f_{\mathrm{scan}} = \alpha_{\mathrm{scan}}\sigma_D = \alpha_{\mathrm{scan}}\sqrt{\gamma T}$ encompasses the full fluorescence line (i.e., that α_{scan} is large and Δf_{scan} is typically much larger than frequency shift Δf employed with the three-frequency technique). Measurements are made at K different, uniformly distributed frequencies that are centered about the fluorescence line. Frequency increment $\Delta f_{\mathrm{scan}}/K$ is comparable to or larger than the laser linewidth. The detected signals are collected as a function of the probing frequency. Let $n_i + b_i$ denote the signal and background noise count in the ith frequency bin, where the average signal count is given by

$$\begin{aligned} \overline{n_i} &\approx \frac{N_T \Delta f_{\mathrm{scan}}/K}{\sqrt{2\pi}\sigma_D} \exp[-(f - f_S)^2/2\sigma_D{}^2], \\ N_T &\approx \sum_{i=1}^{K} \overline{n_i}. \end{aligned} \tag{A6}$$

The mean background noise is subtracted from each bin, and the resultant data are normalized by the Rayleigh signal level at a lower altitude. The temperature is then inferred from the normalized counts. We assume for simplicity that the Rayleigh count is large and is identical for each frequency bin such that the temperature is inferred from the data $n_i + \Delta b_i$, where $\Delta b_i = b_i - \overline{b_i}$ is the uncertainty in the background noise in the ith frequency bin and $\overline{b_i}$ is the average background noise count.

A purely Gaussian line shape is uniquely determined by three parameters: linewidth σ_D, center frequency f_S, and amplitude or area of the fluorescence line N_T. Fitting a Gaussian line shape to the measured photon counts is statistically equivalent to computing sample mean-square linewidth $\hat{\sigma}_D{}^2$, sam-

ple centroid frequency $\hat{f}_S$, and sample total photon count $\hat{N}_T$:

$$\hat{\sigma}_D{}^2 = \frac{\sum_{i=1}^{K} (n_i + \Delta b_i)(f_i - \hat{f}_S)^2}{\sum_{i=1}^{K} (n_i + \Delta b_i)},$$

$$\hat{f}_S = \frac{\sum_{i=1}^{K} (n_i + \Delta b_i) f_i}{\sum_{i=1}^{K} (n_i + \Delta b_i)},$$

$$\hat{N}_T = \sum_{i=1}^{K} (n_i + \Delta b_i). \tag{A7}$$

One can easily determine the temperature error

$$\Delta T = (\sigma_D{}^2 - \hat{\sigma}_D{}^2)/\gamma = \Delta\hat{\sigma}_D{}^2/\gamma \tag{A8}$$

from these equations by noting that the signal and background noise counts are Poisson distributed random variables. It is convenient to express the temperature error in terms of the equivalent signal and background noise that would be achieved if the laser were tuned all the time to the peak of the fluorescence spectrum at frequency f_S:

$$N_S = K \frac{N_T \Delta f_{\text{scan}}/K}{\sqrt{2\pi}\sigma_D} = \frac{N_T \Delta f_{\text{scan}}}{\sqrt{2\pi}\sigma_D} = \frac{\alpha_{\text{scan}} N_T}{\sqrt{2\pi}},$$

$$N_B = \sum_{i=1}^{K} \overline{b_i} = k\bar{b}. \tag{A9}$$

We assume that the mean background noise is the same for each frequency bin because the receiver is not tuned. The rms temperature error for the frequency-scanning technique is given by

$$\Delta T_{\text{rms}}|_{\text{freq-scan}} \approx \frac{T}{\sqrt{N_S}} \left[\sqrt{\frac{2}{\pi}}\, \alpha_{\text{scan}} + \frac{2}{\pi}\, \alpha_{\text{scan}}{}^2 \times \left(1 - \frac{\alpha_{\text{scan}}{}^2}{6} + \frac{\alpha_{\text{scan}}{}^4}{80} \right) \frac{N_B}{N_S} \right]^{1/2}. \tag{A10}$$

During the nighttime, when the background noise is negligible, the temperature error reduces to

$$\Delta T_{\text{rms}}|_{\text{freq-scan/night}} \approx \frac{T}{\sqrt{\text{SNR}_S}} \left(\sqrt{\frac{2}{\pi}}\, \alpha_{\text{scan}} \right)^{1/2}. \tag{A11}$$

During the daytime, when the background count is typically much larger than the signal count, the temperature error is

$$\Delta T_{\text{rms}}|_{\text{freq-scan/day}} \approx \frac{T}{\sqrt{\text{SNR}_S}} \left[\frac{2}{\pi}\, \alpha_{\text{scan}}{}^2 \times \left(1 - \frac{\alpha_{\text{scan}}{}^2}{6} + \frac{\alpha_{\text{scan}}{}^4}{80} \right) \right]^{1/2}, \tag{A12}$$

where in both cases $\alpha_{\text{scan}} = \Delta f_{\text{scan}}/\sigma_D$,

$$\text{SNR}_S = \frac{N_S{}^2}{N_S + N_B}, \tag{A13}$$

and $N_B \ll N_S$ at night.

The error performance of the scanning technique depends critically on the parameter α_{scan}. The analysis assumes that the scan encompasses the majority of the fluorescence line. If $\alpha_{\text{scan}} = 6$, the signal level at the extreme ranges of the scan in the wings of the spectrum at $f = f_S \pm 3\sigma_D$ is 1.1% of the signal at the peak of the fluorescence line, so error formulas given by relations (A11) and (A12) should apply. In this case, compared with the optimized three-frequency technique, the frequency-scanning technique has a 1.7-dB performance penalty at night and a 13-dB penalty during the day.

The author thanks Xinzhao Chu and Alan Liu for their constructive comments and for their help preparing the figures and tables. This study was supported in part by the National Science Foundation.

References

1. L. B. Elterman, "The measurement of the stratospheric density distribution with the search light technique," J. Geophys. Res. **56,** 509–520 (1951).
2. L. B. Elterman, "A series of stratospheric temperature profiles obtained with the searchlight technique," J. Geophys. Res. **58,** 519–530 (1953).
3. L. B. Elterman, "Seasonal trends of temperature, density, and pressure to 67.6 km obtained with the searchlight probing technique," J. Geophys. Res. **59,** 351–358 (1951).
4. D. Bruneau, A. Garnier, A. Hertzog, and J. Porteneuve, "Wind-velocity lidar measurements by use of a Mach–Zehnder interferometer, comparison with a Fabry–Perot interferometer," Appl. Opt. **43,** 173–182 (2004).
5. A. Hauchecorne, M. L. Chanin, and P. Keckhut, "Climatology and trends of middle atmospheric temperatures (33–87 km) as seen by Rayleigh lidar over the south of France," J. Geophys. Res. **96,** 15297–15309 (1991).
6. M. R. Bowman, A. J. Gibson, and M. C. W. Sandford, "Atmospheric sodium measured by a tuned laser radar," Nature **221,** 456–457 (1969).
7. Y. Zhao, A. Liu, and C. S. Gardner, "Measurements of atmospheric stability in the mesopause region at Starfire Optical Range, NM," J. Atmos. Solar Terr. Phys. **65,** 219–232 (2003).
8. R. E. Bills, C. S. Gardner, and C. Y. She, "Narrowband lidar technique for Na temperature and Doppler wind observations of the upper atmosphere," Opt. Eng. **30,** 13–21 (1991).
9. X. Chu, G. Papen, W. Pan, C. S. Gardner, and J. Gelbwachs, "Fe Boltzmann temperature lidar: design, error analysis, and first results from the North and South Poles," Appl. Opt. **41,** 4400–4410 (2002).
10. U. von Zahn and J. Hoffner, "Mesopause temperature profiling by potassium lidar," Geophys. Res. Lett. **26,** 141–144 (1996).
11. R. J. States and C. S. Gardner, "Thermal structure of the mesopause region (80–105 km) at 40 °N latitude. 2. Diurnal variations," J. Atmos. Sci. **57,** 78–92 (2000).
12. C. Y. She, S. Chen, B. P. Williams, Z. Hu, D. A. Krueger, and M. E. Hagan, "Tides in the mesopause region over Ft. Collins, Colorado (41 °N, 105 °W) based on lidar temperature observations covering full diurnal cycles," J. Geophys. Res. **107,** 4350, doi:10.1029/2001JD001189 (2002).
13. W. Pan and C. S. Gardner, "Seasonal variations of the atmo-

spheric temperature structure at South Pole," J. Geophys. Res. **108,** 4564, doi:10.1029/2002JD003217 (2003).
14. A. Corney, *Atomic and Laser Spectroscopy* (Oxford U. Press, Oxford, UK, 1977).
15. G. C. Papen, W. M. Pfenninger, and D. M. Simonich, "Sensitivity analysis of Na narrowband wind-temperature lidar systems," Appl. Opt. **34,** 480–498 (1995).
16. G. C. Papen, C. S. Gardner, and W. M. Pfenninger, "Analysis of a potassium lidar system for upper-atmosphere wind-temperature measurements," Appl. Opt. **34,** 6950–6958 (1995).
17. J. S. Friedman, C. A. Tepley, S. Raizada, Q. H. Zhou, J. Hedin, and R. Delgado, "Potassium Doppler-resonance lidar for the study of the mesosphere and lower thermosphere at the Arecibo Observatory," J. Atmos. Solar Terr. Phys. **65,** 1411–1424 (2003).
18. J. Lautenbach and J. Höffner, "Scanning iron temperature lidar for mesopause temperature observation," Appl. Opt. **43,** 4559–4563 (2004).
19. A. J. Gibson, L. Thomas, and S. K. Bhattachacharyya, "Lidar observations of the ground-state hyperfine structure of sodium and of temperatures in the upper atmosphere," Nature **281,** 131–132 (1979).
20. K. H. Fricke and U. von Zahn, "Mesopause temperature derived from probing the hyperfine structure of the D_2 resonance line of sodium by lidar," J. Atmos. Terr. Phys. **47,** 499–512 (1985).
21. C. Y. She, R. E. Bills, H. Latifi, J. R. Yu, R. J. Alvarez II, and C. S. Gardner, "Two frequency lidar technique for mesospheric sodium temperature measurements," Geophys. Res. Lett. **17,** 929–932 (1990).
22. R. E. Bills, C. S. Gardner, and S. F. Franke, "Na Doppler/temperature lidar: initial mesopause region observations and comparison with the Urbana MF radar," J. Geophys. Res. **96,** 22701–22707 (1991).
23. C. Y. She and J. R. Yu, "Simultaneous three-frequency Na lidar measurements of radial wind and temperature in the mesopause region," Geophys. Res. Lett. **21,** 1771–1774 (1994).
24. J. A. Gelbwachs, "Iron Boltzmann factor lidar: proposed new remote sensing technique for mesospheric temperature," Appl. Opt. **33,** 7151–7156 (1994).
25. C. S. Gardner, G. C. Papen, X. Chu, and W. Pan, "First lidar observations of middle atmosphere temperatures, Fe densities, and polar mesospheric clouds over the North and South Poles," Geophys. Res. Lett. **28,** 1199–1202 (2001).
26. C. S. Gardner, "Sodium resonance fluorescence lidar applications in atmospheric science and astronomy," Proc. IEEE **77,** 408–418 (1989).
27. J. M. C. Plane, C. S. Gardner, J. R. Yu, C. Y. She, R. R. Garcia, and H. C. Pumphrey, "Mesospheric Na layer at 40 °N: modeling and observations," J. Geophys. Res. **104,** 3773–3788 (1999).
28. R. J. States and C. S. Gardner, "Structure of the mesospheric Na layer at 40 °N latitude: seasonal and diurnal variations," J. Geophys. Res. **104,** 11783–11798 (1999).
29. T. J. Kane and C. S. Gardner, "Structure and seasonal variability of the nighttime mesospheric Fe layer at mid-latitudes," J. Geophys. Res. **98,** 16875–16886 (1993).
30. S. Raizada and C. A. Tepley, "Seasonal variation of mesospheric iron layers at Arecibo: first results from low-latitudes," Geophys. Res. Lett. **30,** 1082, doi:10.1029/2002GL016537 (2003).
31. V. Eska, J. Hoffner, and U. von Zahn, "Upper atmosphere potassium layer and its seasonal variations at 54 °N," J. Geophys. Res. **103,** 29207–29214 (1998).
32. J. S. Friedman, S. C. Collins, R. Delgado, and P. A. Castleberg, "Mesospheric potassium layer over the Arecibo Observatory, 18.3 °N 66.75 °W," Geophys. Res. Lett. **29,** 1071, doi:10.1029/2001GL013542 (2002).
33. C. Granier, J. P. Jegou, and G. Megie, "Atomic and ionic calcium in the Earth's upper atmosphere," J. Geophys. Res. **94,** 9917–9924 (1989).
34. J. Qian and C. S. Gardner, "Simultaneous lidar measurements of mesospheric Ca, Na and temperature profiles at Urbana, IL," J. Geophys. Res. **100,** 7753–7461 (1995).
35. M. Alpers, J. Hoffner, and U. von Zahn, "Upper atmosphere Ca and Ca^+ at mid-latitudes: first simultaneous and common-volume lidar observations," Geophys. Res. Lett. **23,** 567–570 (1996).
36. M. Gerding, M. Alpers, U. von Zahn, R. J. Rollason, and J. M. C. Plane, "Atmospheric Ca and Ca^+ layers: midlatitude observations and modeling," J. Geophys. Res. **105,** 27131–27146 (2000).
37. C. S. Gardner, T. J. Kane, D. C. Senft, J. Qian, and G. Papen, "Simultaneous observations of sporadic E, Na, Fe and Ca^+ layers at Urbana, Illinois: three case studies," J. Geophys. Res. **98,** 16865–16873 (1993).
38. R. Beer, "Transmission through the atmosphere," in *Laser Remote Chemical Analysis*, R. M. Measures, ed., Vol. 94 of Chemical Analysis (Wiley, New York, 1985), pp. 85–162.
39. A. Mercherikunnel and C. H. Duncan, "Total and spectral solar irradiance measured at ground surface," Appl. Opt. **21,** 554–556 (1982).
40. W. K. Pratt, *Laser Communication Systems* (Wiley, New York, 1968).
41. L. Delbouille, L. Neven, and C. Roland, *Photometric Atlas of the Solar Spectrum from 3000 to 10,000* (Institut d'Astrophysique de l'Universite de Liege, Observatoire Royal de Belgique, Brussels, Belgium 1973).
42. J. F. Grainger and J. Ring, "Anamolous Fraunhofer line profiles," Nature **193,** 762 (1962).
43. M. Conde, P. Greet, and F. Jacka, "The Ring effect in the sodium D_2 Fraunhofer line of day skylight over Mawson, Antarctica," J. Geophys. Res. **97,** 11561–11565 (1992).
44. C. S. Gardner and W. Yang, "Measurements of the dynamical cooling rate associated with the vertical transport of heat by dissipating gravity waves in the mesopause region at the Starfire Optical Range, NM," J. Geophys. Res. **103,** 16909–16927 (1998).
45. C. Y. She, S. Chen, Z. Hu, J. Sherman, J. D. Vance, V. Vasoli, M. A. White, J. Yu, and D. W. Krueger, "Eight-year climatology of nocturnal temperature and sodium density in the mesopause region (80 to 105 km) over Ft. Collins, CO (41 °N, 105 °W)," Geophys. Res. Lett. **27,** 3289–3292 (2000).
46. J. S. Friedman, "Tropical mesopause climatology over Arecibo Observatory," Geophys. Res. Lett. **30,** doi:10.1029/2003GL016966 (2003).
47. C. Fricke-Begemann, J. Hoffner, and U. von Zahn, "The potassium density and temperature structure in the mesopause region (80–105 km) at low latitude (28 °N)," Geophys. Res. Lett. **29,** doi:10.1029/2002GL015578 (2002).
48. J. Höffner, J. Lautenbach, C. Fricke-Begemann, and P. Menzel, "Observation of temperature, NLC, PMSE and potassium at Svalbard, 78 °N," presented at the 30th Annual European Meeting on Atmospheric Studies by Optical Methods, Longyearbyen, Svalbard, 13–17 August 2003.
49. X. Chu, G. J. Nott, P. J. Espy, C. S. Gardner, J. C. Diettrich, M. A. Clilverd, and M. J. Jarvis, "Lidar observations of polar mesospheric clouds at Rothera, Antarctica (67.5 °S, 68.0 °W)," Geophys. Res. Lett. **31,** L02114, doi:10.1029/2003GL018638 (2004).
50. C. Fricke-Begemann, M. Alpers, and J. Hoffner, "Daylight rejection with a new receiver for potassium resonance temperature lidars," Opt. Lett. **27,** 1932–1934 (2002).
51. D. L. Snyder, *Random Point Processes* (Wiley, New York, 1975).